RESEARCH ARTICLE

NANO · MICRO small
www.small-journal.com

In Situ, Rapid Synthesis of Carbon-Loaded High Density and Ultrasmall High Entropy Oxide Nanoparticles as Efficient Electrocatalysts

Rui Chang, Hongdong Li, Xiaofeng Tian, Yu Yang, Tian Dong, Zhenhui Wang, Jianping Lai, Shouhua Feng, and Lei Wang**

High entropy materials offer almost unlimited catalytic possibilities due to their variable composition, unique structure, and excellent electrocatalytic performance. However, due to the strong tendency of nanoparticles to coarsen and agglomerate, it is still a challenge to synthesize nanoparticles using simple methods to precisely control the morphology and size of the nanoparticles in large quantities, and their large-scale application is limited by high costs and low yields. Herein, a series of high-entropy oxides (HEOs) nanoparticles with high-density and ultrasmall size (<5 nm) loaded on carbon nanosheets with large quantities are prepared by Joule-heating treatment of gel precursors in a short period of time (≈60 s). Among them, the prepared $(FeCoNiRuMn)_3O_{4-x}$ catalyst shows the best electrocatalytic activity for oxygen evolution reaction, with low overpotentials (230 mV @10 mA cm^{-2}, 270 mV @100 mA cm^{-2}), small Tafel slope (39.4 mV dec^{-1}), and excellent stability without significant decay at 100 mA cm^{-2} after 100 h. The excellent performance of $(FeCoNiRuMn)_3O_{4-x}$ can be attributed to the synergistic effect of multiple elements and the inherent structural stability of high entropy systems. This study provides a more comprehensive design idea for the preparation of efficient and stable high entropy catalysts.

1. Introduction

High-entropy materials (HEM), as a new type of catalytic material, are usually composed of five or more major metal elements, which can provide multiple elemental active sites on the surface.[1] Compared with traditional materials, it has better selectivity, stability, and catalytic activity, and shows good development potential in the field of electrocatalysis.[2] And, ultrasmall nanoparticles (NPs) have also attracted extensive research interest in the field of electrocatalysis. With the reduction of nanoparticle size, the utilization efficiency of nanoparticle atoms can be substantially improved and more active sites can be generated, thus enabling the catalyst to have higher catalytic activity.[3] However, due to the tendency of aggregation and thermodynamic instability of ultrasmall NPs, especially at high temperatures,[4] limiting their wide application in practical processes.

Previously reported HEM synthesis methods are mainly based on heat treatment in muffle and tube furnaces, which require long heating, holding, and cooling processes,[5] and long-term pyrolysis at high temperatures tends to lead to agglomeration and sintering of particles, resulting in a larger nanoparticle.[6] Alternatively, the anchor is customized to prepare ultrasmall nanoparticles by doping heteroatoms or introducing highly defective substrates.[7] However, these methods usually lead to relatively complex synthesis conditions and low nanoparticle loadings. In recent years, the preparation of HEM by the fast Joule heating method has received wide attention.[8] Joule heating has become a promising method for the synthesis of a wide range of catalysts due to its ultrafast heating and cooling rates, which allow precise heating control in a short period of time, instantaneous formation of homogeneous phases of disordered metallic elements with nanometer-sized particle sizes, and reduced energy consumption.[9] Moreover, in order to improve the performance of the catalyst, a more simple and controllable method is urgently needed, which can realize the preparation of high-entropy NPs with ultrasmall size and high loading.

In this work, we use a combination of liquid-phase sol–gel method and vapor-phase thermal treatment to prepare high-density, ultrasmall, HEOs NPs loaded on carbon flakes in large quantities by rapid thermal treatment of viscous gel precursors in a short period of time (≈60 s). The method combines the

R. Chang, H. Li, X. Tian, Y. Yang, T. Dong, Z. Wang, J. Lai, S. Feng, L. Wang
Key Laboratory of Eco-Chemical Engineering
International Science and Technology Cooperation Base of Eco-Chemical Engineering and Green Manufacturing
College of Chemistry and Molecular Engineering
Qingdao University of Science and Technology
Qingdao 266042, P. R. China
E-mail: lihd@qust.edu.cn; inorchemwl@qust.edu.cn
L. Wang
Shandong Engineering Research Center for Marine Environment Corrosion and Safety Protection
College of Environment and Safety Engineering
Qingdao University of Science and Technology
Qingdao 266042, P. R. China

The ORCID identification number(s) for the author(s) of this article can be found under https://doi.org/10.1002/smll.202309937

DOI: 10.1002/smll.202309937

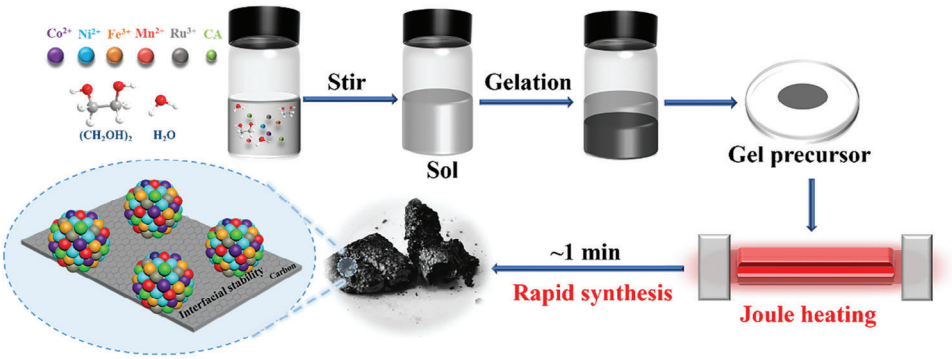

Figure 1. Schematic illustration of the rapid Joule heating process applied on gel precursor and corresponding HEOs products.

advantages of liquid-phase synthesis, i.e., solution processability, homogeneity, and large-scale production, which allows for the preparation of HEOs NPs in large quantities with high efficiency, and the prepared NPs are free of impurities, avoiding the complex debinding process. In addition, in order to prevent the agglomeration of NPs, we use Joule heat to rapidly synthesize the carbon substrate, so that the ultrasmall NPs are uniformly dispersed on the carbon substrate in high density. Among them, the $(FeCoNiRuMn)_3O_{4-x}$ catalysts exhibited low overpotentials (230 mV at 10 mA cm^{-2}, 270 mV at 100 mA cm^{-2}), high mass activity (3.01 A mg^{-1}), low Tafel slopes (39.4 mV dec^{-1}) and excellent long-term (100 h) electrocatalytic stability in 1 M KOH solution. This "fast-heating gel precursor" strategy provides a practical and feasible way to produce large quantities of homogeneous, high-density, ultra-small nanoparticles in a fast, efficient, and simple way.

2. Results and Discussion

First, we successfully prepared a series of HEOs with spinel structure by gel and fast Joule-heating strategy (**Figure 1**). In this process, we mixed citric acid (CA) with metal nitrates, which led to the formation of polybasic chelates by complexation between —COOH groups in CA and metal ions,[10] followed by esterification with ethylene glycol (EG) to generate cross-linked polyesters in which the metal ions were uniformly immobilized within the polymer network. The obtained cross-linked polyester mixture was aged at a high temperature, which in turn gave the desired gel precursor. By rapid heat treatment of the gel precursor in a vacuum using a Joule heating device, the gel precursor undergoes rapid dehydration and violent redox reactions, and a large amount of gas release (e.g., H_2O, CO) and rapid volume expansion is observed. In the meantime, the gas generated rapidly blows the precursors into bubbles and the polymer walls of the generated bubbles turn into solid carbon at high temperatures. They then become nanosheets after the bubbles rupture and/or collapse. Meanwhile, by controlling the heating time (≈60 s) and temperature (≈400 °C), the nuclei of MOs are able to grow freely into ultrasmall nanoparticles, forming carbon sheets loaded with high-density, ultrasmall, high-entropy oxide nanoparticles (Figure S1, Supporting Information). The key to the experiment is to control the time and temperature of the heat treatment reaction, which ensures the proper chemical reaction and physical expansion kinetics. The morphology and structure of $(FeCoNiRuMn)_3O_{4-x}$ were characterized by scanning electron microscopy (SEM) and transmission electron microscopy (TEM). The SEM images (**Figure 2a**; Figure S2, Supporting Information) exhibit that the material is carbon sheet loaded with high-density and ultrasmall nanoparticles and that the samples are uniform in morphology. The TEM image (Figure 2b) further confirms that the nanoparticles are uniformly distributed on the carbon, and the diameter of the prepared $(FeCoNiRuMn)_3O_{4-x}$ NPs is about 4.32 ± 0.07 nm (Figure 2c). The dispersed ultrasmall nanoparticles not only expose more active sites and accelerate electron transfer but also promote the release of generated O_2. The high-resolution TEM (HRTEM) images of $(FeCoNiRuMn)_3O_{4-x}$ (Figure 2d–f) display that the lattice spacing is 0.21 nm, corresponding to the (400) plane. The crystal structure of $(FeCoNiRuMn)_3O_{4-x}$ was further revealed by X-ray diffraction (XRD) (Figure 2g), and the resulting samples showed distinct diffraction peaks at 35.4, 43.1, and 62.6°, which corresponded to the (311), (400), and (440) planes of spinel $CoFe_2O_4$ (PDF#22-1086), respectively. In addition, further analysis of the distribution of each element in $(FeCoNiRuMn)_3O_{4-x}$ by TEM-mapping (Figure 2h) shows that all elements (C, Fe, Co, Ni, Ru, Mn, O) are uniformly distributed, which is consistent with the SEM-mapping results (Figure S3, Supporting Information). Meanwhile, the EDS result indicates that the metal-atom ratio of the synthesized HEOs is approximated to be 1:1:1:1:1 and the ratio of all metal atoms to oxygen atoms is about 3:4, which is in agreement with the XPS result (Table S1, Supporting Information), confirming the elemental composition of the samples as well as the homogeneity of the elemental mixing of the $(FeCoNiRuMn)_3O_{4-x}$. Through the above characterization, the successful preparation of high entropy oxides $(FeCoNiRuMn)_3O_{4-x}$ was demonstrated.

To further explore the surface valence states of the $(FeCoNiRuMn)_3O_{4-x}$, X-ray photoelectron spectroscopy (XPS) tests were performed (**Figure 3**; Figure S4, Supporting Information). All elemental data were calibrated with the C 1s peak at 284.8 eV. The high-resolution XPS spectra of Ni 2p, Fe 2p, Co 2p, Ru 3p, Mn 2p, and O 1s of $(FeCoNiRuMn)_3O_{4-x}$ are shown in Figure 3. Among them, the electronegativity differences of Fe(1.83), Co(1.88), Ni(1.91), Ru(2.20) and Mn(1.55) cause significant charge redistribution. Figure 3a shows the XPS spectrum of Ni 2p, the characteristic peaks are attributable to the coexistence of Ni^{2+} (855.2 and 873.0 eV for Ni^{2+} $2p_{3/2}$ and Ni^{2+}

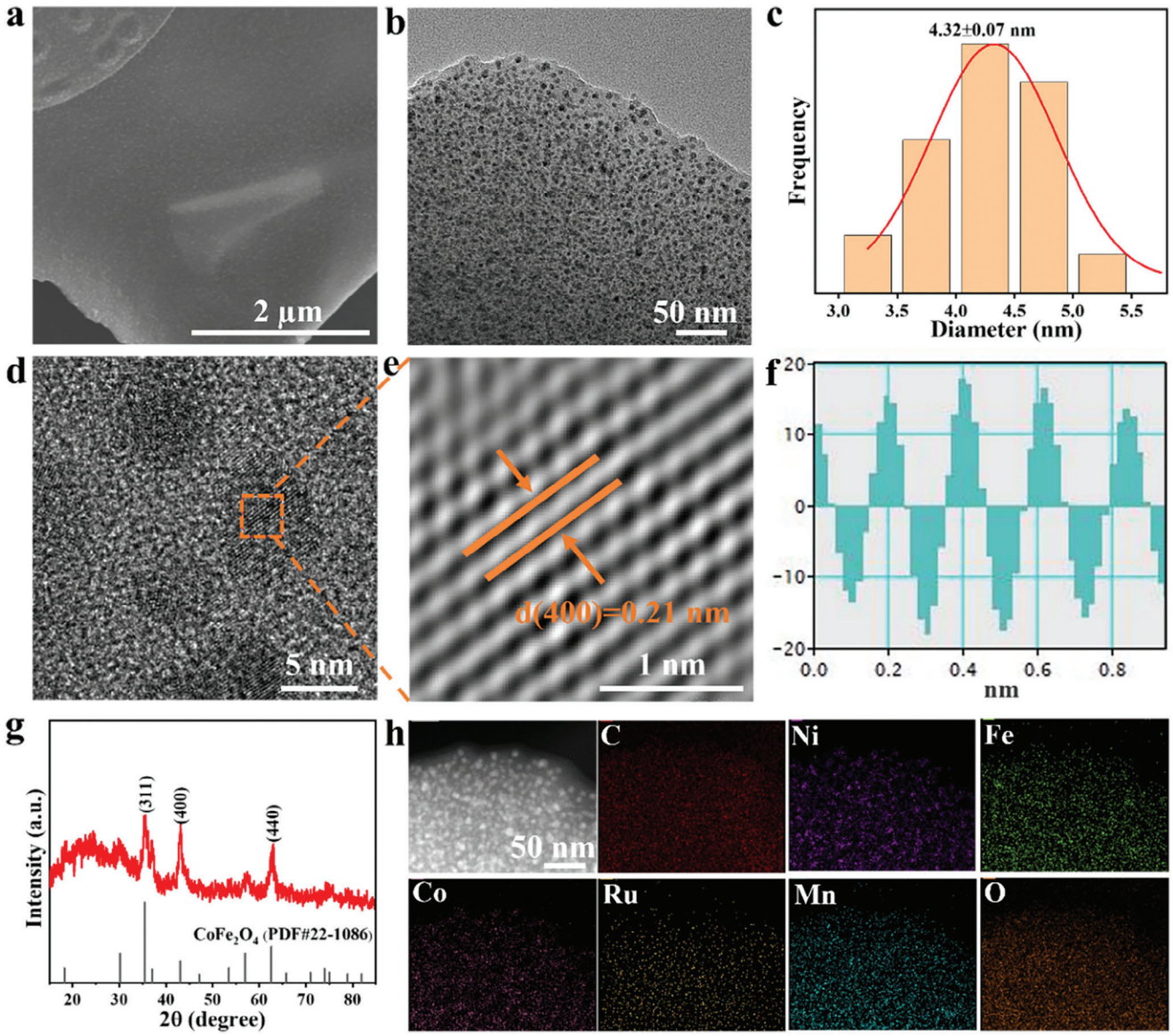

Figure 2. a) SEM image, b) TEM image, c) nanoparticle size distribution, d) HRTEM image, e) Atomic resolution images show d spacings of one random area labeled in (d), f) Intensity profile of (400) planes, g) The XRD pattern, and h) TEM image and the corresponding elemental mappings of $(FeCoNiRuMn)_3O_{4-x}$.

$2p_{1/2}$, respectively) and Ni^{3+} (856.7 and 874.6 eV for Ni^{3+} $2p_{3/2}$ and Ni^{3+} $2p_{1/2}$, respectively). The peaks of Fe $2p_{3/2}$ (711.9 eV and 714.8 eV) and Fe 2p1/2 (723.8 eV and 726.1 eV) can be divided into two peaks, corresponding to Fe^{2+} and Fe^{3+}, respectively (Figure 3b). For the Co 2p spectra (Figure 3c), the characteristic peaks can be divided into Co^{3+} (780.8 eV and 796.6 eV for Co^{3+} $2p_{3/2}$ and Co^{3+} $2p_{1/2}$, respectively) and Co^{2+} (782.6 eV and 797.9 eV for Co^{2+} $2p_{3/2}$ and Co^{2+} $2p_{1/2}$, respectively). As shown in Figure 3d, the peak of Ru is divided into two peaks at 462.1 eV and 484.3 eV, corresponding to Ru^{4+} $3p^{3/2}$ and Ru^{4+} $3p^{1/2}$, respectively. The Mn 2p spectrum (Figure 3e) shows the coexistence of $Mn^{2+/3+}$ $2p_{3/2}$ (641.9 eV), $Mn^{2+/3+}$ $2p_{3/2}$ (653.4 eV), Mn^{4+} $2p_{3/2}$ (644.3 eV) and Mn^{4+} $2p_{3/2}$ (655.1 eV). The above results show that compared with $(FeCoNi)_3O_{4-x}$ and $(FeCoNiMn)_3O_{4-x}$, Co, Ni, Fe, and Mn in $(FeCoNiRuMn)_3O_{4-x}$ move in the direction of high binding energy, respectively, indicating that Ru acts as an electron acceptor and increases the electron density of Ru site. This can promote nucleophilic attacks of water molecules, thereby lowering the kinetic barrier of OER.[11] In addition, due to the great difference in electronegativity between Ru and other transition metals, the addition of Ru may also generate a large number of active sites on the surface of high-entropy materials, which is beneficial to OER. For example, active Co and Ru sites can be generated to optimize their energy barriers for the stabilization of OH* and H* intermediates and improve OER activity.[12] For the element oxygen (Figure 3f), the O 1s peak is fitted to the three peaks of lattice oxygen (≈530.1 eV), oxygen vacancy (≈531.5 eV), and chemisorbed oxygen (≈532.9 eV). The

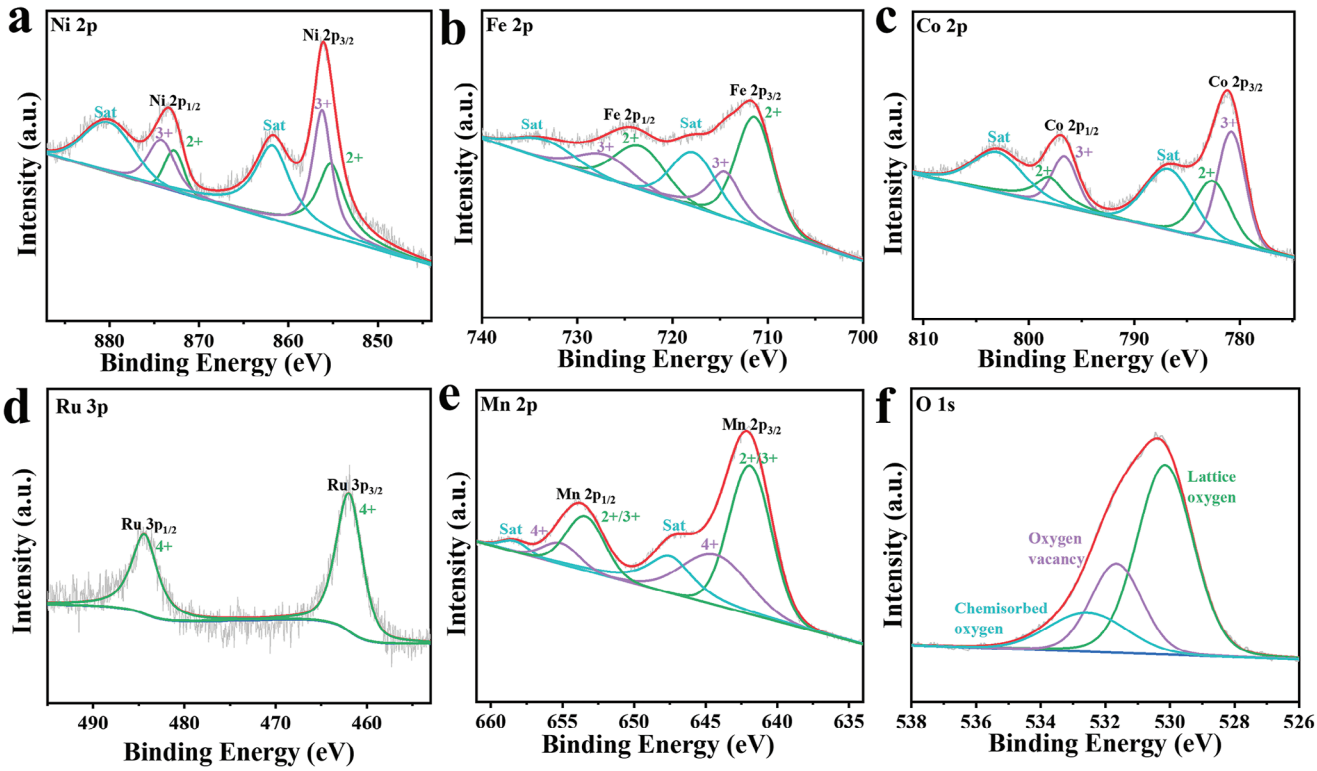

Figure 3. High resolution XPS spectra of a) Ni 2p, b) Fe 2p, c) Co 2p, d) Ru 3p, e) Mn 2p, f) O 1s in $(FeCoNiRuMn)_3O_{4-x}$.

presence of oxygen vacancy can further balance the electronic structure of the entire spinel compound as well as the surface adsorption.[13]

In addition to $(FeCoNiRuMn)_3O_{4-x}$, the $(FeCoNiCrMn)_3O_{4-x}$, $(FeCoNiCuMn)_3O_{4-x}$, $(FeCoNiMn)_3O_{4-x}$, and $(FeCoNi)_3O_{4-x}$ could also be prepared by changing the corresponding metal salts. And SEM, SEM–EDS mapping, and XRD were performed for those HEOs catalysts. The SEM images demonstrated the prepared HEOs had the structure of carbon-loaded high-density and ultrasmall nanoparticles, and elemental mapping further showed a homogeneous distribution of their elements (**Figure 4**; Figures S5 and S7–10, Supporting Information). Meanwhile, XRD comparisons of all the samples (Figure S6, Supporting Information) confirmed that the crystal structures of the prepared samples were all spinel structures and the cation substitution did not lead to significant phase transitions. In addition, fundamentally, due to the different atomic radii of the alloying elements, the alloying of different elements shifts the position of the peaks to different 2θ values, and the addition of Cr or Ru elements to $(FeCoNi)_3O_{4-x}$ forms $(FeCoNiCrMn)_3O_{4-x}$ or $(FeCoNiRuMn)_3O_{4-x}$, which are slightly shifted under the 2θ angle due to the fact that the radii of the Cr and Ru ions are larger than those of Fe, Ni or Co.[8a,14] EDS and XPS consistently show that the catalyst has an approximate metal-atom ratio of 1:1:1:1:1 and an approximate 3:4 ratio of all metal atoms to oxygen atoms, with the same stoichiometric ratio as that of $(FeCoNiRuMn)_3O_{4-x}$ (Figures S7–S10 and Table S1, Supporting Information).

In addition, in order to explore the chemical state of the prepared samples, XPS was also tested, further verifying the characteristics of the HEOs. As can be seen from Figure S13 (Supporting Information), the introduction of low electronegative Mn elements into highly electronegative Fe, Co, and Ni can result in strong local electron interactions caused by electronegative differences and the adsorption energy of reactant intermediates and products was effectively reduced, thus enhancing the alkaline OER performance of the HEOs catalysts. Specifically, low energy shifts also occurred in Ni, Fe, and Co upon Mn doping. These results indicate that the doping of Mn^{2+} resulted in the transfer of electrons from Mn^{2+} to Ni^{2+}, $Fe^{3+,}$ and Co^{2+}. This is because the electronegativity of Mn^{2+} is lower than that of Ni^{2+}, Fe^{3+}, and Co^{2+}, resulting in a weaker ability to attract electrons, and thus electron transfer from Mn^{2+} to Ni^{2+}, Fe^{3+}, and Co^{2+} occurs. In this case, the electron density around the electron acceptor increases, favoring electrocatalysis. In addition, the presence of Mn^{4+} in $(FeCoNiMn)_3O_{4-x}$ may accelerate the electron transfer process and increase the electrical conductivity.[15] In $(FeCoNiCuMn)_3O_{4-x}$, the electronegativity is Mn (1.55) < Fe (1.83) < Co (1.88) < Cu (1.90) < Ni (1.91), and the electronegativity difference between different metals results in strong local electron transfer. From Figure S14 (Supporting Information), it can be seen that Cu and Ni move towards lower binding energies, and Mn, Fe, and Co move towards higher binding energies, resulting in an increase in the localized electron density at the Ni and Cu sites and a decrease in the localized electron density at the Mn, Co, and Fe sites. The inactive Cu can be driven to act as an electron-rich active site for OER, which effectively reduces the adsorption energies of reactants, intermediates, and products, and thus improves the electrocatalytic activity.[3a,16] In $(FeCoNiCrMn)_3O_{4-x}$, the difference in electronegativity leads to

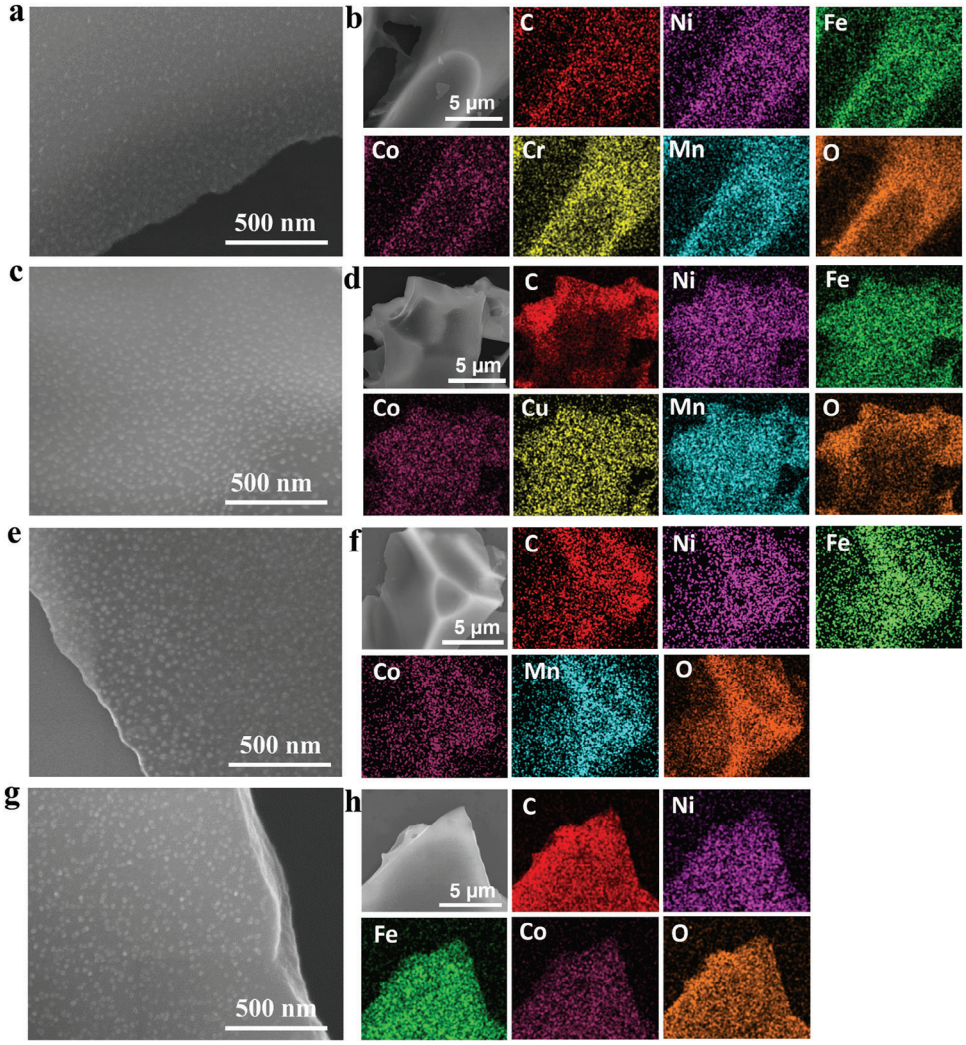

Figure 4. SEM and SEM–EDS elemental mapping images of a,b) $(FeCoNiCrMn)_3O_{4-x}$, c,d) $(FeCoNiCuMn)_3O_{4-x}$, e,f) $(FeCoNiMn)_3O_{4-x}$, and g,h) $(FeCoNi)_3O_{4-x}$ HEOs.

a redistribution of the electron cloud density when these metals form a HEO, and Cr and Mn show lower electronegativity compared to Fe, Co, and Ni, suggesting that the Cr and Mn atoms should provide electrons and contribute significantly to changing the electronic structure. This is consistent with the XPS analysis (Figure S15, Supporting Information), which shows Cr and Mn moving toward higher binding energies and Ni, Fe, and Co moving toward lower binding energies.[17] In addition, the presence of Cr has been shown to increase the OER activity of the material. The introduction of Cr, which has a strong effect on the oxidation state of the Fe, Ni, and Co-active sites, enhances the OER activity by promoting a high oxidation state of the active elements (Co, Ni, and Fe). In addition, Cr and Mn have higher oxidation states of Cr^{6+} and Mn^{4+}, respectively. This change in valence cannot be explained simply by considering electronegativity but involves complex modifications of electronic structures. However, catalysts with high oxidation states tend to favor electrocatalytic activity. Thus, $(FeCoNiCrMn)_3O_{4-x}$ has a favorable OER activity.[8a,18]

Transition metal compounds, especially oxides, including Fe, Co, and Ni elements, have excellent OER activity, which has been confirmed by previous reports.[19] The HEOs exhibit excellent catalytic properties due to the interaction of multiple metal elements. Therefore, to further investigate the electrocatalytic performance of the synthesized catalysts, the synthesized HEOs were tested and investigated as OER electrocatalysts in a 1.0 M KOH solution. **Figure 5a** shows the LSV curves of the four prepared HEOs electrocatalysts and commercial RuO_2 in 1.0 M KOH solution, and it can be seen that the $(FeCoNiRuMn)_3O_{4-x}$ catalyst has the best OER activity. From the Figure 5b, $(FeCoNiRuMn)_3O_{4-x}$ exhibits the smallest overpotentials at 10 mA cm^{-2} (230 mV) and 100 mA cm^{-2} (270 mV) in 1 m KOH solution, which are superior to $(FeCoNiCrMn)_3O_{4-x}$ (300 mV at 10 mA cm^{-2}, 359 mV at 100 mA cm^{-2}), $(FeCoNiCuMn)_3O_{4-x}$ (310 mV at 10 mA cm^{-2}, 380 mV at 100 mA cm^{-2}), $(FeCoNiMn)_3O_{4-x}$ (317 mV at 10 mA cm^{-2}, 413 mV at 100 mA cm^{-2}) and $(FeCoNi)_3O_{4-x}$ (330 mV at 10 mA cm^{-2}, 466 mV at 100 mA cm^{-2}). Notably, $(FeCoNiRuMn)_3O_{4-x}$

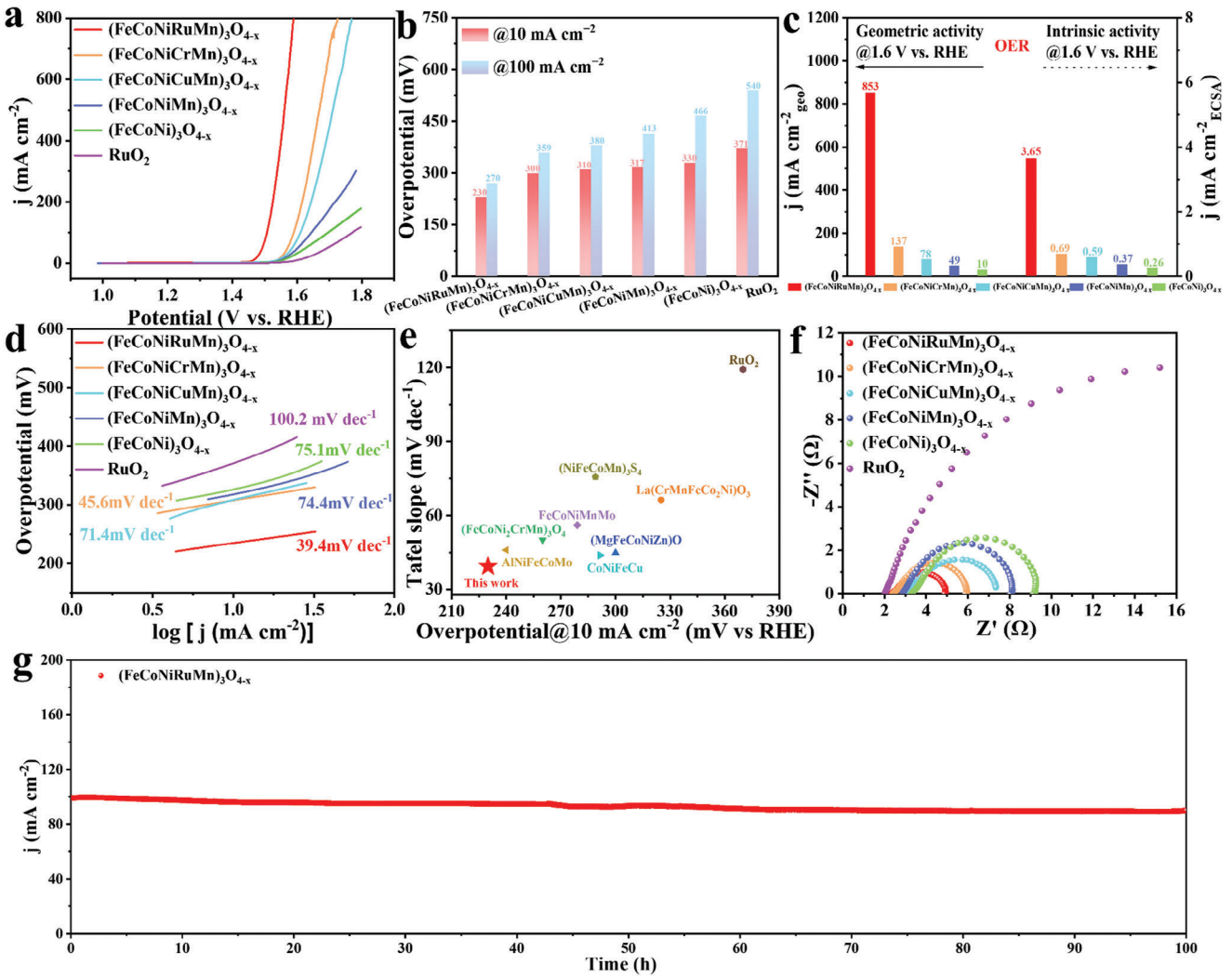

Figure 5. a) OER polarization curves, b) Overpotentials at current densities of 10 and 100 mA cm^{-2}, c) The geometric electrode surface area and ECSA activity, d) Tafel slope values, e) Comparison of the overpotential at 10 mA cm^{-2} and Tafel slope with previously reported electrocatalysts, f) Nyquist plots, g) The long-term OER stability test of $(FeCoNiRuMn)_3O_{4-x}$ at 100 mA cm^{-2} in 1.0 M KOH solution.

showed lower overpotentials than commercial RuO_2 (371 mV at 10 mA cm^{-2}, 540 mV at 100 mA cm^{-2}), which further suggests that $(FeCoNiRuMn)_3O_{4-x}$ possesses optimal electrocatalytic OER activity.

Achieving high current densities at low overpotentials is crucial for practical applications. The anodic current density of $(FeCoNiRuMn)_3O_{4-x}$ at an overpotential η = 370 mV is 853 mA cm^{-2}, which exceeds that of $(FeCoNiCrMn)_3O_{4-x}$ (137 mA cm^{-2}), $(FeCoNiCuMn)_3O_{4-x}$ (78 mA cm^{-2}), $(FeCoNiMn)_3O_{4-x}$ (49 mA cm^{-2}), and $(FeCoNi)_3O_{4-x}$ (10 mA cm^{-2}) catalysts. Moreover, the electrochemical surface area (ECSA) of the samples was evaluated by calculating the double-layer capacitance (C_{dl}) values, and cyclic voltammetry (CV) curves of the samples at different scan rates (10, 20, 30, 40, and 50 mV s^{-1}) were recorded (Figures S16 and S17, Supporting Information). The C_{dl} values of $(FeCoNiRuMn)_3O_{4-x}$, $(FeCoNiCrMn)_3O_{4-x}$, $(FeCoNiCuMn)_3O_{4-x}$, $(FeCoNiMn)_3O_{4-x}$, and $(FeCoNi)_3O_{4-x}$ in 1.0 M KOH solution are 9.35, 7.89, 5.32, 5.28, and 4.98 mF cm^{-2}, respectively, indicating that $(FeCoNiRuMn)_3O_{4-x}$ has more active sites than other HEOs. Interestingly, when the overpotential η = 370 mV, the $(FeCoNiRuMn)_3O_{4-x}$ (3.65 mA $cm^{-2}{}_{ECSA}$) catalyst exhibited a higher intrinsic activity than the $(FeCoNiCrMn)_3O_{4-x}$ (0.69 mA $cm^{-2}{}_{ECSA}$), $(FeCoNiCuMn)_3O_{4-x}$ (0.59 mA $cm^{-2}{}_{ECSA}$), $(FeCoNiMn)_3O_{4-x}$ (0.37 mA $cm^{-2}{}_{ECSA}$) and $(FeCoNi)_3O_{4-x}$ (0.26 mA $cm^{-2}{}_{ECSA}$) catalysts. Both the geometric activity and intrinsic activity (Figure 5c; Figure S18, Supporting Information) indicated that the synthesized $(FeCoNiRuMn)_3O_{4-x}$ catalysts had better OER activity than $(FeCoNiCrMn)_3O_{4-x}$, $(FeCoNiCuMn)_3O_{4-x}$, $(FeCoNiMn)_3O_{4-x}$ and $(FeCoNi)_3O_{4-x}$. Furthermore, when the overpotential is 370 mV, the mass activity (Figure S19, Supporting Information) of $(FeCoNiRuMn)_3O_{4-x}$ is 3.01 A mg^{-1}, which is greater than that of $(FeCoNiCrMn)_3O_{4-x}$ (0.51 A mg^{-1}), $(FeCoNiCuMn)_3O_{4-x}$ (0.30 A mg^{-1}), $(FeCoNiMn)_3O_{4-x}$ (0.15 A mg^{-1}), and $(FeCoNi)_3O_{4-x}$ (0.13 A mg^{-1}). The Tafel slope

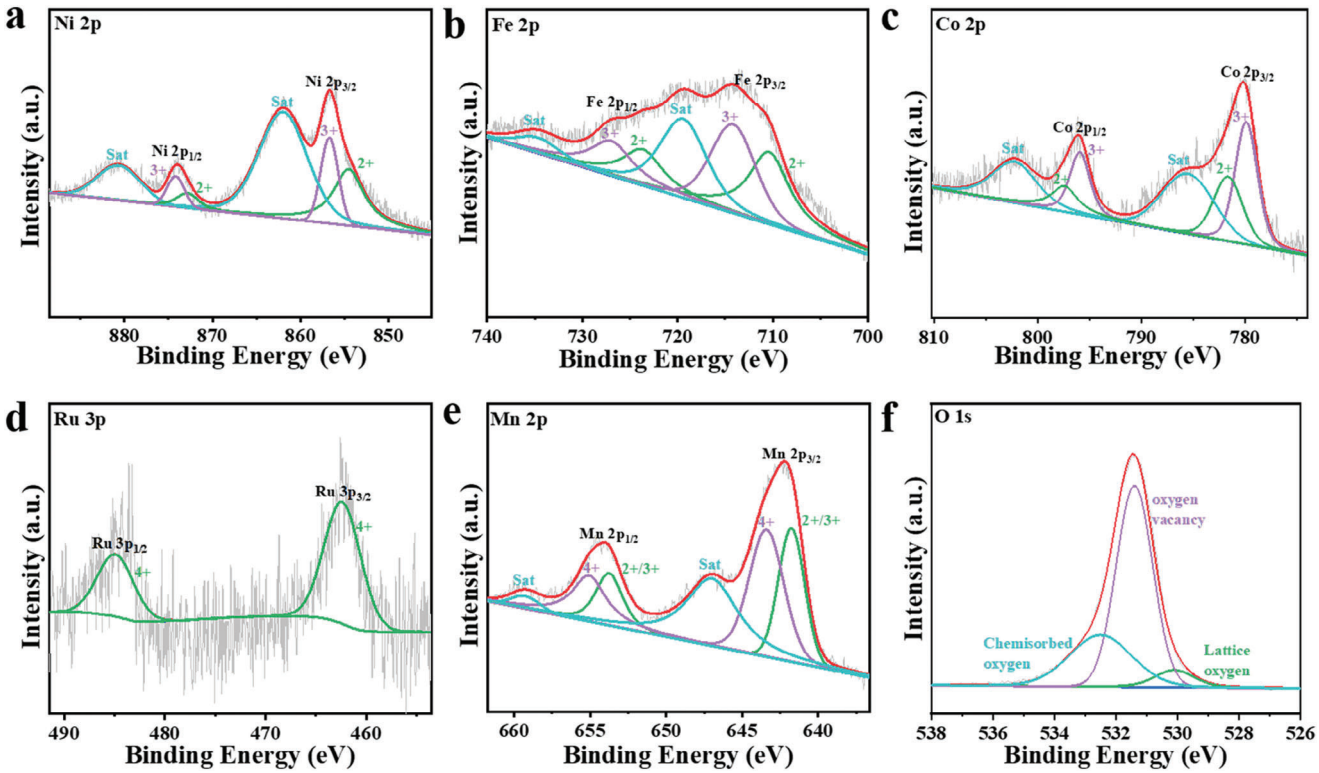

Figure 6. High-resolution XPS spectra of a) Ni 2p, b) Fe 2p, c) Co 2p, d) Ru 3p, e) Mn 2p, f) O 1s in $(FeCoNiRuMn)_3O_{4-x}$ after the stability test.

is also an important indicator of the electrocatalytic performance. The smaller Tafel slope indicates better kinetics of the catalyst for OER. In 1.0 m KOH solution, $(FeCoNiRuMn)_3O_{4-x}$ only showed a low Tafel slope of 39.4 mV dec^{-1} (Figure 5d), which was much lower than that of $(FeCoNiCrMn)_3O_{4-x}$ (45.6 mV dec^{-1}), $(FeCoNiCuMn)_3O_{4-x}$ (71.4 mV dec^{-1}), $(FeCoNiMn)_3O_{4-x}$ (74.4 mV dec^{-1}), $(FeCoNi)_3O_{4-x}$ (75.1 mV dec^{-1}), and RuO_2 (100.2 mV dec^{-1}).

To reveal the reaction kinetics of HEOs, the electrochemical impedance spectroscopy (EIS) was measured. The EIS test (Figure 5f) results show that $(FeCoNiRuMn)_3O_{4-x}$ has the smallest charge transfer resistance and is much smaller than that of the commercial RuO_2 catalysts, indicating a faster charge transfer rate during OER electrocatalysis. In order to further explore the intrinsic OER activity of HEOs with different elements, the turnover frequency (TOF) curves (Figure S20, Supporting Information) were calculated with all metals as active sites. At 370 mV overpotential, the TOF value of $(FeCoNiRuMn)_3O_{4-x}$ is 0.508 s^{-1}, which is much larger than that of $(FeCoNiCrMn)_3O_{4-x}$ (0.074 s^{-1}), $(FeCoNiCuMn)_3O_{4-x}$ (0.044 s^{-1}), $(FeCoNiMn)_3O_{4-x}$ (0.021 s^{-1}) and $(FeCoNi)_3O_{4-x}$ (0.019 s^{-1}), indicating that the addition of Ru elements can effectively improve the catalytic activity of HEOs. In summary, $(FeCoNiRuMn)_3O_{4-x}$ has the advantages of low overpotential, small Tafel slope, high mass activity, and fast charge transfer rate, which showed the best OER catalytic performance in the prepared HEOs samples, and the OER activity of $(FeCoNiRuMn)_3O_{4-x}$ catalysts is better than most noble metal catalysts and non_precious metal catalysts (Figure 5e; Table S2, S3, Supporting Information).

The stability of electrocatalysts is crucial in practical applications, and we have investigated the long_term OER stability of $(FeCoNiRuMn)_3O_{4-x}$ catalysts by means of continuous time–current profiles. As shown in Figure 5g, $(FeCoNiRuMn)_3O_{4-x}$ remained stable at a high current density of 100 mA cm^{-2} for more than 100 h with excellent stability. The excellent electrocatalytic stability of the prepared samples can be attributed to the difficult aggregation of NPs loaded on the carbon sheet in situ and the inherent structural stability of HEOs.

In order to understand the stability of the catalysts during the catalytic process, the $(FeCoNiRuMn)_3O_{4-x}$ catalysts tested for stability were analyzed by SEM, TEM, and XRD. As shown by SEM and TEM images (Figure S21a–d and S22, Supporting Information), $(FeCoNiRuMn)_3O_{4-x}$ maintains the original microstructure of carbon-loaded high–density and ultrasmall high-entropy oxide nanoparticles after stability tests and mapping images show that all elements are uniformly distributed. Moreover, the XRD spectra of $(FeCoNiRuMn)_3O_{4-x}$ showed that there were no separated XRD peaks of the metal oxides after the catalytic reaction (Figure S21e, Supporting Information). These results show that the crystal structure and morphology of the high-entropy materials remain unchanged after the reaction, which proves that it has excellent stability.

The surface valence states of $(FeCoNiRuMn)_3O_{4-x}$ after stability testing were further characterized by XPS (**Figure 6**). The ratio of $Mn^{2+/3+}$ in the $(FeCoNiRuMn)_3O_{4-x}$ catalysts was significantly reduced, indicating that some of the metal elements in the lower state were transformed to the higher valence state, a process that can activate the oxygen ions and provide more active sites for the

OER reaction. The O 1s XPS spectrum (Figure S23, Supporting Information) shows that the proportion of lattice oxygen is significantly reduced, indicating that lattice oxygen is involved in the reaction. In order to verify the conjecture and to deeply investigate the catalytic mechanism of the catalysts, we performed LSV tests on the samples in KOH solutions of different pH (12.5, 13, 13.5, 14). As shown in Figure S24 (Supporting Information), the OER activity of $(FeCoNiRuMn)_3O_{4-x}$ increased significantly with the increase of KOH solution pH, indicating that solution pH is an important factor affecting the catalytic activity of the catalyst. In order to accurately illustrate the relationship between activity and pH, we used the proton reaction order (ρ^{RHE}) to reflect the dependence of the OER reaction kinetics on the proton activity. When the ρ^{RHE} value is close to 1, it indicates that $(FeCoNiRuMn)_3O_{4-x}$ exhibits a strong PH dependence during OER.[17] This apparent dependence of the catalytic activity on the pH of the alkaline solution demonstrates the involvement of lattice oxygen in the O—O coupling during the reaction, which is consistent with the XPS results of O1s and the lattice oxygen-mediated mechanism (LOM). In addition, tetramethylammonium (TMA) cation was also used to recognize LOM as it can form strong electrostatic interactions with O2 and thus retard the LOM process.[20] The catalytic process was tested with 1 m TMAOH instead of 1 m KOH electrolyte. The activity of $(FeCoNiRuMn)_3O_{4-x}$ in 1 m TMAOH decreased significantly compared with 1 m KOH (Figure S25, Supporting Information), suggesting that OER is limited by TMA^+. Thus, it is demonstrated that the reaction is driven by both AEM and LOM and that the oxygen vacancy contributes significantly to the increase in electrocatalytic activity. The increase of oxygen vacancies can not only optimize the coordination environment of the metal centers, but also improve the electrical conductivity of the catalyst, accelerate the absorption intermediates of OER, and effectively improve the OER performance.[17]

3. Conclusion

In summary, a series of carbon-loaded high-density, ultrasmall HEO nanoparticles $(FeCoNiXMn)_3O_{4-x}$ (X = Ru, Cr, Cu), $(FeCoNiMn)_3O_{4-x}$ and $(FeCoNi)_3O_{4-x}$ were prepared by a gel and rapid joule heating method. Subsequent OER performance tests demonstrated that those materials have excellent catalytic activity under alkaline conditions, where the $(FeCoNiRuMn)_3O_{4-x}$ exhibits the best catalytic activity (230 mV at 10 mA cm^{-2}, 270 mV at 100 mA cm^{-2}), and low Tafel slopes (39.4 mV dec^{-1}), superior to most of the reported transition metal oxides. In addition, the $(FeCoNiRuMn)_3O_{4-x}$ also shows excellent stability, operating at 100 mA cm^{-2} for 100 h has almost no attenuation. This excellent performance can be attributed to the abundance of active sites, synergistic interactions between different elements, and entropic stabilization mechanisms. This work provides a simple method for the synthesis of high-sensitivity and ultrasmall NPs and provides an effective way to develop economical and efficient HEO electrocatalysts.

Supporting Information

Supporting Information is available from the Wiley Online Library or from the author.

Acknowledgements

This work was supported by the National Natural Science Foundation of China (Nos. 52072197 and 21971132), Youth Innovation and Technology Foundation of Shandong Higher Education Institutions, China (No. 2019KJC004), Outstanding Youth Foundation of Shandong Province, China (No. ZR2019JQ14), Major Scientific and Technological Innovation Project (No. 2019JZZY020405), Major Basic Research Program of Natural Science Foundation of Shandong Province under Grant (No. ZR2020ZD09), Qingdao Postdoctoral Researcher Applied Research Project (No. QDBSH20220202043).

Conflict of Interest

The authors declare no conflict of interest.

Data Availability Statement

The data that support the findings of this study are available from the corresponding author upon reasonable request.

Keywords

high density, high-entropy oxides, Joule-heating, oxygen evolution reaction, ultrasmall

Received: November 1, 2023
Revised: December 15, 2023
Published online:

[1] a) Y. Yao, Q. Dong, A. Brozena, J. Luo, J. Miao, M. Chi, C. Wang, I. G. Kevrekidis, Z. J. Ren, J. Greeley, G. Wang, A. Anapolsky, L. Hu, *Science* **2022**, *376*, eabn3103; b) H. Li, J. Lai, Z. Li, L. Wang, *Adv. Funct. Mater.* **2021**, *31*, 2106715; c) M. W. Glasscott, A. D. Pendergast, S. Goines, A. R. Bishop, A. T. Hoang, C. Renault, J. E. Dick, *Nat. Commun.* **2019**, *10*, 2650; d) J. Masa, C. Andronescu, W. Schuhmann, *Angew. Chem., Int. Ed.* **2020**, *59*, 15298.

[2] a) H. Li, Y. Han, H. Zhao, W. Qi, D. Zhang, Y. Yu, W. Cai, S. Li, J. Lai, B. Huang, L. Wang, *Nat. Commun.* **2020**, *11*, 5437; b) K. Zeng, J. Zhang, W. Gao, L. Wu, H. Liu, J. Gao, Z. Li, J. Zhou, T. Li, Z. Liang, B. Xu, Y. Yao, *Adv. Funct. Mater.* **2022**, *32*, 2204643; c) Y. Yao, Z. Liu, P. Xie, Z. Huang, T. Li, D. Morris, Z. Finfrock, J. Zhou, M. Jiao, J. Gao, Y. Mao, J. Miao, P. Zhang, R. Shahbazian-Yassar, C. Wang, G. Wang, L. Hu, *Sci. Adv.* **2020**, *6*, eaaz0510; d) Y. Chida, T. Tomimori, T. Ebata, N. Taguchi, T. Ioroi, K. Hayashi, N. Todoroki, T. Wadayama, *Nat. Commun.* **2023**, *14*, 4492; e) X. Li, Y. Zhou, C. Feng, R. Wei, X. Hao, K. Tang, G. Guan, *Nano Res.* **2022**, *16*, 4411; f) T. Mushiana, M. Khan, M. I. Abdullah, N. Zhang, M. Ma, *Nano Res.* **2022**, *15*, 5014.

[3] a) H. Zhu, S. Sun, J. Hao, Z. Zhuang, S. Zhang, T. Wang, Q. Kang, S. Lu, X. Wang, F. Lai, T. Liu, G. Gao, M. Du, D. Wang, *Energy Environ. Sci.* **2023**, *16*, 619; b) J.-H. Cha, S.-H. Cho, D.-H. Kim, D. Jeon, S. Park, J.-W. Jung, I.-D. Kim, S.-Y. Choi, *Adv. Mater.* **2023**, *35*, 2305222; c) Y. Yu, F. Xia, C. Wang, J. Wu, X. Fu, D. Ma, B. Lin, J. Wang, Q. Yue, Y. Kang, *Nano Res.* **2022**, *15*, 7868; d) H. Li, Y. Pan, J. Lai, L. Wang, S. Feng, *Chin. J. Struct. Chem.* **2022**, *41*, 2208003.

[4] a) Q. Dong, M. Hong, J. Gao, T. Li, M. Cui, S. Li, H. Qiao, A. H. Brozena, Y. Yao, X. Wang, G. Chen, J. Luo, L. Hu, *Small* **2022**, *18*, 2104761; b) T. Li, Q. Dong, Z. Huang, L. Wu, Y. Yao, J. Gao, X. Wang, H. Zhang, D. Wang, T. Li, R. Shahbazian-Yassar, L. Hu, *Adv. Mater.* **2022**, *32*, 2106436.

[5] a) H. Wu, Q. Lu, Y. Li, J. Wang, Y. Li, R. Jiang, J. Zhang, X. Zheng, X. Han, N. Zhao, J. Li, Y. Deng, W. Hu, *Nano Lett.* **2022**, *22*, 6492; b) G. Zhong, S. Xu, C. Chen, D. J. Kline, M. Giroux, Y. Pei, M. Jiao, D. Liu, R. Mi, H. Xie, B. Yang, C. Wang, M. R. Zachariah, L. Hu, *Adv. Funct. Mater.* **2019**, *29*, 1904282.

[6] a) W. Shi, Z. Li, Z. Gong, Z. Liang, H. Liu, Y.-C. Han, H. Niu, B. Song, X. Chi, J. Zhou, H. Wang, B. Y. Xia, Y. Yao, Z.-Q. Tian, *Nat. Commun.* **2023**, *14*, 2294; b) T. Li, Y. Yao, B. H. Ko, Z. Huang, Q. Dong, J. Gao, W. Chen, J. Li, S. Li, X. Wang, R. Shahbazian-Yassar, F. Jiao, L. Hu, *Adv. Funct. Mater.* **2021**, *31*, 2010561; c) Y. Liu, X. Tian, Y.-C. Han, Y. Chen, W. Hu, *Chin. J. Catal.* **2023**, *48*, 66; d) H. Li, M. Sun, Y. Pan, J. Xiong, H. Du, Y. Yu, S. Feng, Z. Li, J. Lai, B. Huang, L. Wang, *Appl. Catal. B: Environ.* **2022**, *312*, 121431.

[7] a) J.-Y. Song, C. Kim, M. Kim, K. M. Cho, I. Gereige, W.-B. Jung, H. Jeong, H.-T. Jung, *Sci. Adv.* **2021**, *7*, eabk2984; b) Y. Yao, Z. Huang, P. Xie, T. Li, S. D. Lacey, M. Jiao, H. Xie, K. K. Fu, R. J. Jacob, D. J. Kline, Y. Yang, M. R. Zachariah, C. Wang, R. Shahbazian-Yassar, L. Hu, *ACS Appl. Mater. Interfaces* **2019**, *11*, 29773.

[8] a) A. Abdelhafiz, B. Wang, A. R. Harutyunyan, J. Li, *Adv. Energy Mater.* **2022**, *12*, 2200742; b) Y. Yao, Z. Huang, P. Xie, S. D. Lacey, R. J. Jacob, H. Xie, F. Chen, A. Nie, T. Pu, M. Rehwoldt, D. Yu, M. R. Zachariah, C. Wang, R. Shahbazian-Yassar, J. Li, L. Hu, *Science* **2018**, *359*, 1489.

[9] a) J. Zhao, Z. Wang, X. Fang, L. Yang, C. Wu, W. Gan, Y. Zhou, L. Shan, Y. Lin, *J. Alloys Compd.* **2023**, *966*, 171535; b) Z. Zhao, J. Sun, Z. Li, X. Xu, Z. Zhang, C. Li, L. Wang, X. Meng, *J. Mater. Chem. A.* **2023**, *11*, 10346; c) X. Zheng, X. Gao, R. A. Vilá, Y. Jiang, J. Wang, R. Xu, R. Zhang, X. Xiao, P. Zhang, L. C. Greenburg, Y. Yang, H. L. Xin, X. Zheng, Y. Cui, *Nat. Nanotech* **2022**, *18*, 153.

[10] D. Wang, W. Zhou, R. Zhang, J. Zeng, Y. Du, S. Qi, C. Cong, C. Ding, X. Huang, G. Wen, T. Yu, *Adv. Mater.* **2018**, *30*, 1803569.

[11] J. Hao, Z. Zhuang, K. Cao, G. Gao, C. Wang, F. Lai, S. Lu, P. Ma, W. Dong, T. Liu, M. Du, H. Zhu, *Nat. Commun.* **2022**, *13*, 2662.

[12] H. Zhu, Z. Zhu, J. Hao, S. Sun, S. Lu, C. Wang, P. Ma, W. Dong, M. Du, *Chem. Eng. J.* **2022**, *431*, 133251.

[13] Q. Zhang, Y. Hu, H. Wu, X. Zhao, M. Wang, S. Wang, R. Feng, Q. Chen, F. Song, M. Chen, P. Liu, *ACS Nano* **2023**, *17*, 1485.

[14] R. Zhang, Z. Xu, Z. Du, Y. Wan, S. Yuan, F. Zeng, J. Xu, Z. Meng, X. Hu, H. Tian, *Inorg. Chem.* **2023**, *62*, 19052.

[15] M. Han, C. Wang, J. Zhong, J. Han, N. Wang, A. Seifitokaldani, Y. Yu, Y. Liu, X. Sun, A. Vomiero, H. Liang, *Appl. Catal. B: Environ.* **2022**, *301*, 120764.

[16] T. X. Nguyen, Y.-H. Su, C.-C. Lin, J.-M. Ting, *Adv. Funct. Mater.* **2021**, *31*, 2106229.

[17] D. Wang, C. Duan, H. He, Z. Wang, R. Zheng, H. Sun, Y. Liu, C. Liu, *J. Colloid. Interface Sci.* **2023**, *646*, 89.

[18] a) Z.-J. Chen, T. Zhang, X.-Y. Gao, Y.-J. Huang, X.-H. Qin, Y.-F. Wang, K. Zhao, X. Peng, C. Zhang, L. Liu, M.-H. Zeng, H.-B. Yu, *Adv. Mater.* **2021**, *33*, 2101845; b) P. Ma, S. Zhang, M. Zhang, J. Gu, L. Zhang, Y. Sun, W. Ji, Z. Fu, *Sci. China Mater.* **2020**, *63*, 2613.

[19] a) I. A. Cechanaviciute, R. P. Antony, O. A. Krysiak, T. Quast, S. Dieckhöfer, S. Saddeler, P. Telaar, Y.-T. Chen, M. Muhler, W. Schuhmann, *Angew. Chem., Int. Ed.* **2023**, *62*, 202218493; b) S.-P. Zeng, H. Shi, T.-Y. Dai, Y. Liu, Z. Wen, G.-F. Han, T.-H. Wang, W. Zhang, X.-Y. Lang, W.-T. Zheng, Q. Jiang, *Nat. Commun.* **2023**, *14*, 1811; c) H. Liao, G. Ni, P. Tan, K. Liu, X. Liu, H. Liu, K. Chen, X. Zheng, M. Liu, J. Pan, *Adv. Mater.* **2023**, *35*, 2300347.

[20] F. Wang, P. Zou, Y. Zhang, W. Pan, Y. Li, L. Liang, C. Chen, H. Liu, S. Zheng, *Nat. Commun.* **2023**, *14*, 6019.